Weighted kernel mapping model with spring simulation based watershed transformation for level set image segmentation

Yingchun Zhang[a,*], He Guo[a], Feng Chen[b], Hongji Yang[c]

[a] *School of Software Technology, Dalian University of Technology, China*
[b] *School of Computer Science and Informatics, De Montfort University, UK*
[c] *Centre for Creative Computing, Bath Spa University, UK*

Abstract

This paper proposes a novel active contour model called weighted kernel mapping (WKM) model along with an extended watershed transformation (EWT) method for the level set image segmentation, which is a hybrid model based on the global and local intensity information. The proposed EWT method simulates a general spring on a hill with a fountain process and a rainfall process, which can be considered as an image pre-processing step for improving the image intensity homogeneity and providing the weighted information to the level set function. The WKM model involves two new energy functionals which are used to segment the image in the low dimensional observation space and the higher dimensional feature space respectively. The energy functional in the low dimensional space is used to demonstrate that the proposed WKM model is right in theory. The energy functional in the higher dimensional space obtains the region parameters through the weighted kernel function by utilising mean shift technique. Since the region parameters can better represent the values of the evolving regions due to the better image homogeneity, the proposed method can more accurately segment various types of images. Meanwhile, by adding the weighted information, the level set elements can be updated faster and the image segmentation can be achieved with fewer iterations. Experimental results on synthetic, medical and natural images show that the proposed method can increase the accuracy of image segmentation and reduce the iterations of level set evolution for image segmentation.

Keywords: Image segmentation, Level set, Watershed transformation, Intensity

*Corresponding author at: School of Software Technology, Dalian University of Technology, Dalian, China
Email address: Zhangyingchun@mail.dlut.edu.cn (Yingchun Zhang)

inhomogeneity, Spring simulation, Energy functional

1. Introduction

Image segmentation is a fundamental concept in image processing and has been a main subject of many theoretical and practical studies [1–3]. Generally, the purpose of image segmentation is to split an image uniformly into intersected and non-overlapped regions through certain properties such as textures or colours. Therefore, image segmentation can simplify the image representation for image understanding and analysis. Active contour model introduced by Kass et al. [4] is one of the most successful methods for image segmentation. The basic idea is to represent a contour as the zero level set of the level set functionals, and evolve the curve under some constraints to extract the desired objects. Over the past few decades, the active contour models have shown promising results through using level set methods in image segmentation [5–12].

The active contour models by level set methods can be broadly categorised into two basic types: edge-based methods [5–9] and region-based methods [10–22]. The edge-based methods utilise image gradients to drive the level set evolution. For instance, the well-known geodesic active contour (GAC) model [5] uses an edge stopping function to lead the active contour to the object boundaries. The edge-based methods are suitable for the images with strong gradient or high contrast. However, these methods are susceptible to the environmental noises, the location of the initial curve as well as the weak edges [20]. To prevent these limitations, the region-based methods exploit the regional information such as intensities and textures inside and outside the evolving contour to guide the contour evolution.

The region-based active contour model assumes that the image in each region is statistically homogeneous [10–13]. In the early years, the most prominent representative of region-based models for image segmentation was Mumford-Shah (MS) model [23]. However, minimising the Mumford-Shah (MS) energy functional is arduous and time-consuming, and hence, some simplified versions of MS model have been proposed [12, 13]. Among them, the Chan-Vese (CV) model is one of the most representative and popular region-based models, and has been extended in various ways [15–18]. Nowadays, the region-based models can be mainly classified into two groups: global region-based models [12–14, 16] and local region-based models [15, 17, 18, 22].

Intensity inhomogeneity occurs in many real-world images. The global region-based model may fail to handle the images with intensity inhomogeneity by only using global statistics. To solve this problem, the local region-based model assumes that an image with intensity inhomogeneity is intensity inhomogeneous in

global region, but its each local region is approximated to be intensity homogeneous. In this way, the local region-based model can extract the local regional information to incorporate into the level set energy functional. The Local Binary Fitting (LBF) model [15] based on the kernel function utilises the averages of local intensities to approximate the image intensities inside and outside of the curve to guide the contour evolution. The Bias Correction based Local Binary Fitting (BCLBF) model [18] is an integration of the LBF model with multiplicative model of intensity inhomogeneity, and simultaneously uses the estimated bias field to correct the intensity inhomogeneity. The Local Images Fitting (LIF) model [17] introduces the local fitted image energy functional to extract the local information, then uses the Gaussian filtering to regularise the level set function. Huang et al. [22] proposed a modified BCLBF model (MBCLBF) to improve the segmentation results of the images with intensity inhomogeneity. Comparing with the global region-based models, the local region-based models are more complex and time-consuming [16].

In order to make use of the advantages of both global and local models but overcome the disadvantages of them, some hybrid models have been proposed [24, 25] by combining the global and local region-based information. Zhou et al. [24] adopted a weighting function to combine a global energy term and a local energy term so that the produced hybrid model could improve the efficiency and accuracy of medical image segmentation. This hybrid model could not handle various types of images. Wang et al. [25] utilised the global region-based model to preliminarily segment the image and get a coarse segmentation, and then used the local region-based model to further segment the image. This hybrid method could improve the accuracy of the segmentation, but could not improve the efficiency. Moreover, it could only be used for the two-phase segmentation.

The level set image segmentation by the kernel mapping (KM) model [16] is a global region-based model, which can segment various types of images, including images with slight intensity inhomogeneity. However, the KM model is not suitable for segmenting images with severe intensity inhomogeneity, such as computed tomography (CT) and magnetic resonance (MR) images. In other words, the KM model produces more inaccurate segmentation results than the local region-based models for images with severe intensity inhomogeneity.

Motivated by the problems mentioned above and inspired by hybrid models as well as kernel mapping method, a weighted kernel mapping (WKM) model along with a novel extended watershed transformation (EWT) method based on the spring simulation for the level set image segmentation is proposed in this research. Unlike the existing methods in the literature that the corrected image [18, 22] can be obtained in the level set evolving process, the proposed approach utilises the EWT method to process the image with intensity inhomogeneity or

noise before the level set evolution. The weighted information for performing the level set image segmentation will be prepared via the EWT process as well. The WKM model involves two new energy functionals in the low dimensional observation space and the higher dimensional feature space respectively. The energy functional in the low dimensional observation space is a new global region-based model, which can be used to demonstrate the correctness of the proposed WKM model in theory. The weighted information from the EWT process is used to construct a weighted kernel mapping function. The energy functional in the higher dimensional feature space is a new local region-based model by applying the weighted kernel mapping function onto the global region-based model, which can obtain the region parameters through the weighted kernel function and then guide the motion of the zero level set towards the object boundaries. Several popular kernel functions are capable of clustering the data of complex structure properly [26, 27]. Namely, the image segmentation is spatially constrained clustering of image data. The weighted kernel mapping function can transform nonlinear separable data into linear separable data [28]. In this way, the image that cannot be accurately segmented in the low dimensional space can be accurately segmented in the higher dimensional space by applying the weighted kernel mapping function. Being a hybrid model, the proposed approach can effectively deal with various types of images. In this paper, some kinds of images including the natural images from Berkeley database, the brain images from Normal Brains Database, as well as some artificial images are tested and evaluated. In summary, the main contributions of this work are listed as follows:

a. An extended watershed transformation(EWT) based on spring simulation is proposed and its algorithm is presented. The extended watershed transformation manages to improve the image homogeneity and provide the weighted information for the level set function of the WKM model.

b. Two new energy functionals in the low dimensional observation space and the higher dimensional feature space are designed respectively. The theoretical proof based on the energy functional in the low dimensional space is given.

c. By combining the EWT method, a weighted kernel mapping (WKM) model for level set image segmentation is proposed, which leads to better segmentation accuracy and iterative efficiency. The main experiments for multi-phase image segmentation further demonstrate the desirable performance of the WKM model.

The remainder parts of this paper are organised as follows: Section 2 reviews the related work on level set image segmentation. Section 3 introduces traditional watershed transformation in image segmentation. Section 4 describes the proposed level set image segmentation approach and its implementations. The experimental results are evaluated in Section 5 and the conclusions are drawn in Section 6.

2. Relate work for level set image segmentation

In this section, three classical level set image segmentation models: KM, LIF and BCLBF [16–18] are reviewed and discussed. The LIF and BCLBF models are two popular local region-based level set image segmentation models, while the KM model is a global region-based level set image segmentation model. The discussion here focuses on the energy functionals and their time complexity.

2.1. The LIF model

For an image I in an image domain Ω, the energy functional of the LIF model is defined as follows:

$$E^{LIF}(u) = \frac{1}{2}\int_{\Omega} |I(x) - I^{LFI}(u(x))|^2 dx, x \in \Omega \tag{1}$$

$$I^{LFI} = m_1 H_\varepsilon(u) + m_2(1 - H_\varepsilon(u)) \tag{2}$$

where m_1 and m_2 meet the following conditions:

$$m_1 = mean(I(x) \in \{u(x) > 0, and, x \in W_k\}) \tag{3}$$

$$m_2 = mean(I(x) \in \{u(x) < 0, and, x \in W_k\}) \tag{4}$$

where W_k is a rectangular Gaussian window. The level set evolution equation is:

$$\frac{\partial u}{\partial t} = (I - I^{LFI})(m_1 - m_2)\delta_\varepsilon(u) \tag{5}$$

Note that in Eqs.(1)-(5), $H_\varepsilon(u)$ and $\delta_\varepsilon(u)$ are Heaviside function and Dirac function respectively, $u(x)$ indicates the level set function. The LIF model has three characteristics. First, the local fitted image (LFI) formulation is defined to extract the local image information. Second, the Gaussian filter is used to regularise the level set function and eliminate the requirement of re-initialisation for each iteration. Last, the traditional regularised term is removed because the level set function of the LIF model has been smoothed by using the Gaussian filter. In this way, the LIF model has less computational complexity to finish the image segmentation than other local region-based models [15, 18]. However, the LIF model is sensitive to the local region scale and the initial contour, and easy to produce segmentation errors.

The time complexity of the LIF model: in every iteration, the computing of the LIF model includes the updating of the region parameters, the level set, and the regularisation term in every iteration. Since the LIF model uses Gaussian

kernel to regularise the level set, the traditional regularised term can be removed. The time complexity of Gaussian filtering is $O(gl*gl*N)$. According to literature [17], gl indicates the parameter of Gaussian filtering, where $1 < gl < 6$. The time complexity of updating every region parameter is $O(gw * gw * N)$, where gw indicates the size of Gaussian window. According to Section 3.1 of literature [17], $gw \geq 5$. The time complexity of updating the level set is $O(N)$. Therefore, the time complexity for every iteration of the LIF model is $O((gl * gl + 2 * gw * gw + 1) * N)$.

2.2. The BCLBF model

For an image I with an image domain Ω, the energy functional of the BCLBF model is defined as follows:

$$E(u, c, b) = \int \sum_{i=1}^{N} e_i(x) M_i(u(x)) dx + \int R(u(x)) dx, x \in \Omega \tag{6}$$

where N=2 and $e_i(x)$ is given as follows:

$$e_i(x) = \int K(y - x) |I(x) - b(y)c_i|^2 dy \tag{7}$$

The level set evolution equation is deduced as follows:

$$\frac{\partial u}{\partial t} = (e_1 - e_2)\delta_\varepsilon(u) + R(u(x)) \tag{8}$$

In the above Eqs.(6) and (8), $M_i(u)$ and $\delta_\varepsilon(u)$ are Heaviside function and Dirac function respectively, where $M_1(u) = H_\varepsilon(u)$ and $M_2(u) = 1 - H_\varepsilon(u)$. The BCLBF model presents the bias field estimation to correct the image with intensity inhomogeneities. c indicates the region parameter, b is referred to as a bias field. $e_i(x)$ is a local clustering criterion function to evaluate the classification of intensities in neighbourhood of a pixel. The smaller value of $e_i(x)$ implies the better classification. $R(u(x))$ is referred to as a regularisation term (see literature [18] for more details). Although this model has been well applied to some kinds of medical images with inhomogeneity and noise under high contrast between the foreground and the background, it does not consider the clustering variance, which may cause unsatisfied segmentation for the images with severe intensity inhomogeneity [21].

The time complexity of the BCLBF model: in every iteration, the computing of the BCLBF model includes the updating of the region parameters, the level set, the bias field term and its two gaussian kernel convolutions, as well as the regularised term which contains the curvature term and the penalty term. The time complexity of the curvature term is $O(8N)$, whereas the time complexity of the penalty term is $O(4N)$. So the time complexity of the regularised term is

$O(12N)$. The time complexity of the bias field term and its two gaussian kernel convolutions is $O(3 * gn * gn * N)$, where gn indicates the parameter of truncated Gaussian function, $gn \geq 3$. The time complexity of updating the level set and the region parameters is $O(3N)$. Therefore the time complexity for every iteration of the BCLBF model is $O((15 + 3 * gn * gn) * N)$.

2.3. The KM model

Let $\varphi(.)$ be a nonlinear mapping function. The energy function of the KM model is defined as follows:

$$F_K(R_1, R_2, \mu_1, \mu_2) = \int_{R_1} ||\varphi(I(x)) - \varphi(\mu_1)||^2 dx$$

$$+ \int_{R_2} ||\varphi(I(x)) - \varphi(\mu_2)||^2 dx + \lambda \oint_{\vec{\gamma}} ds \tag{9}$$

where the first two terms are data driven terms, the last term is a regularisation term used for smoothing segmentation boundaries, λ is a positive constant. The level set evolution equation is defined as follows:

$$\frac{\partial u}{\partial t}(x,t) = [||\varphi(I(x)) - \varphi(\mu_1)||^2 -$$

$$||\varphi(I(x)) - \varphi(\mu_2)||^2 - \lambda k_u]||u|| \tag{10}$$

where k_u is a curvature function. More details are available in [16]. The basic idea is to shift the problem of image segmentation from the low dimensional observation space to the higher dimensional feature space. The energy functional of the CV model is defined as follows:

$$F(R_1, R_2, C_1, C_2) = \lambda_1 \int_{R_1} ||(I(x)) - (C_1)||^2 dx$$

$$+\lambda_2 \int_{R_2} ||(I(x)) - (C_2)||^2 dx + \lambda \oint_{\vec{\gamma}} ds \tag{11}$$

where $\lambda_1 = 1$ and $\lambda_2 = 1$, C_1 and C_2 indicate the average gray value of region R_1 and region R_2. The KM model can be essentially viewed as a variant of the CV model, which the curve evolution is only implemented in higher dimensional space. Because the KM model adopts the kernel mapping function, it can effectively segment many types of homogeneous images. However it cannot obtain satisfactory segmentation result for images with narrow part of the object, or images with severe intensity inhomogeneity [16].

The time complexity of the KM model: in every iteration, the computing of the KM model includes the updating of the curvature, the gradient, the region parameters and the level set elements. The time complexity of updating the curvature is $O(8N)$. The time complexity of updating the gradient is $O(8N)$. The time complexity of updating the region parameters and the level set is $O(3N)$. Therefore the time complexity for every iteration of the KM model is $O(19N)$.

3. Review of two classical watershed transformations

In this section, definitions and basic ideas of traditional watershed transformation are reviewed in literature [29–32].

For an image I with an image domain Ω, $x \in \Omega$, $I(x)$ indicates the gray value of pixel x. The watershed transformation is defined as follows:

Definition 1. *The catchment basin $CB(m_i)$ of a regional minimum m_i is a set of points $x \in \Omega$ which are closer to m_i than to any other regional minimum m_j in the topographical distance [29–32].*

Definition 2. *Watersheds are obtained by piercing a hole at each minimum m_i of an image I. Starting from the minima of lowest altitude, the water will progressively fill up the different catchment basins $CB(m_i)$. A dam is built at each pixel, where the water coming from two or more minima would merge. At the end of the immersion procedure, each minimum is completely surrounded by dams, which delimit its associated catchment basins. The dams are called the watersheds of the image I [29, 30, 32].*

The traditional watershed transformation can be categorised into two approaches: immersion and rainfall.

Vincent and Soille propose a classical watershed algorithm [29] by simulating an immersing process. The main idea: all pixels are sorted in an ascending order of their gray values, the progressive flooding process starts from the minimal gray level, suppose the flooding rises to a given level h, the pixels below the given level h will have been labeled. If the flooding rises to level h + 1, then the pixels with altitude h + 1 will be added the labeled catchment basins by computing geodesic influence zones. Those remained unlabeled pixels of level h + 1 are regarded as new minima, and will be given new labels. Such watershed transformation is very close to the concept of natural watershed.

Bieniek and Moga propose a distinct watershed algorithm [31] which is implemented by simulating a rainfall process, not an immersing process as usual. The basic idea: Simulates pouring down water from top (as raining) on topographic surface. It is regarded as a distributed approach since every droplet follows, independently from neighbouring droplets, the steepest descent until reaching a minimum. This process continues for every droplet that falls on the surface and stops when each point is allocated to a minimum. All droplets that follow to the same local minimum form a catchment basin. No point belongs to a watershed line; instead each point is considered as belonging to a particular catchment basin. Compared with the immersion, this algorithm is faster and can segment the image completely.

4. The proposed approach

In this section, a weighted kernel mapping approach to image segmentation is proposed as shown in Fig. 1. An extended watershed transformation method based on spring simulation is introduced and its corresponding algorithm is presented to preprocess the image data. The extended watershed transformation can provide the weighted information for evolving level set and updating region parameters, and reduce the impact of intensity inhomogeneity. Two energy functionals in low dimensional observation space and higher dimensional feature space are designed. The weighted kernel mapping energy functional in higher dimensional space is minimised by means of the weighted level set evolution to guide the motion of the zero level set towards the object boundaries.

4.1. The extended watershed transformation based on spring simulation

Inspired by the immersion simulation [29, 30] and the rainfall simulation [31], an extended watershed transformation method is proposed in this research to simulate a general spring on a hill with a fountain process and a rainfall process. Every minimum in an image is regarded as a spring. Although the actual maximum of jetting height of each spring may be different, the same upper bound of jetting height are set for all the springs. It is supposed that the water will stop jetting when the water level reaches the maximum jetting height. The rising of the water level can be treated as an immersion process, while the falling back of spring water can be viewed as a local rainfall process. The area of local rainfall will at least cover the area of immersion. The immersion process and local rainfall process will construct a catchment basin around a spring. If all gray values of an image are changed to negative values, the local maximum in the original image will become the local minimum in the negative image. If the local maximal point is used as an initial seed point, then the whole catchment basin can be traversed

by using the region growing method without knowing the local minimal pixel point, which can save the time of traversing the seed points. Similar to the traditional watershed transformation, the proposed watershed transformation needs to resolve the problem of water coming from different catchment basins. However, the proposed watershed transformation does not need to erect dams and sort the pixels, but needs to determine to which basin the pixels belong. Unlike the classical watershed transformation methods [29–32] which are used for image segmentation, the proposed watershed transformation method are used for the pre-process of the image segmentation.

For an image I with an image domain Ω, $I(x)$ indicates the gray value of pixel x, $x \in \Omega$. The catchment basin of the extended watershed transformation is defined as follows:

$$ECB(em_i) = \{y | y \in Ng(rm_i), (-1)^{min\_B(em_i)}(I(em_i) - I(y)) \leq d\} \tag{12}$$

$$min\_B(em_i) = \begin{cases} 1, if\ em_i\ take\ the\ local\ minimum \\ 0, otherwise \end{cases}$$

where $Ng(x)$ indicates 4-connected neighbourhoods of pixel x, rm_i indicates any one of pixels which can meet a given condition and be traversed by searching 4-connected neighbourhoods starting from em_i, and em_i can be the local minimum or maximum point.

Suppose that $D(x)$ indicates the image data after the watershed transformation and Mean() denotes the average function. If $x \in ECB(em_i)$ and $ECB(em_i) \subset \Omega$ then $D(x) = Mean(ECB(em_i))$. Here, the loss of image information should be within the tolerance, which means that the image has no visual changes after the extended watershed transformation.

The traditional watershed transformation is sensitive to noise and isolated points. The extended watershed transformation method adds a selective step to resolve this problem. The image is traversed in row-major order. The extreme points can be attained by comparing 8-connected neighborhoods, and then searching 4-connected neighborhoods. Every pixel has at most two chances to be caught by different catchment basins. Such pixel will be added to the closest catchment basin.

The algorithm for the extended watershed transformation is shown in the following steps:

Input: original image

Output: new image and weighted matrix

Step 1: Build three null matrixes with the same size of the original image. The variable L is used as a counter and initialised to zero. The first matrix (Mt1(x)) is used to save the label of every pixel. The second matrix (Mt2(x)) is

used to store the weight of every pixel. The third matrix (Mt3(x)) is used to save the extremum of every catchment basin before the last step, and then is used to store the average value of every catchment basin in the last step.

Step 2: Traverse the image in row-major order. Select an extremum point em_i by comparing a pixel with 8-connected neighborhoods; get points meeting the condition of Eq.(12) by searching 4-connected neighborhoods from this extreme point, $ECB(em_i) = ECB(em_i) \bigcup x$; update the corresponding labels in the first and the third matrix, $L = L + 1$, $Mt1(ECB(em_i)) = L$, $Mt3(ECB(em_i)) = I(em_i)$.

Step 3: Repeat step 2 until the traversing is over. If a pixel y has been added to a catchment basin $ECB(em_i)$, for catchment basin $ECB(em_j)$, if $|I(y) - I(em_i))| > |I(y) - I(em_j)|$, then the pixel y will be added in the $ECB(em_j)$.

Step 4: Search all pixels which are labeled as zero or the outliers (L=1) in Mt1. According the original image and Mt3, these pixels will be added to the closest catchment basin by 8-connected neighborhoods comparison.

Step 5: According to Mt1, compute the weight of every pixel in Mt2 and update Mt3, if $x \in ECB(em_j)$ then Mt3(x)=Mean($ECB(em_j)$). Output the weighted matrix Mt2 and the new image Mt3.

Here Mt2(x) can be viewed as $|D_p(x)|$ and its calculation is given in next subsection. Mt3(x) also indicates D(x) mentioned above.

Fig. 2 is an example that shows the results using extended watershed transformation with different values of d from Eq.(12). The result equals the original image when $d = 0$. The image has barely visual change and presents better intensity homogeneity when $d = 5$. If the value of d is too large, the strong edges will appear in the image as illustrated in Fig. 2(c) and (d). In other words, after the extended watershed transformation the image will have better intensity homogeneity so long as the parameter d is carefully adjusted.

4.2. The weighted information

Let's suppose $|D_p(x)|$ indicates the number of pixels from $D_p(x)$, $D_P(x) = \{y|if\ x \in ECB(em_i),\ then\ \forall y \in ECB(em_i)\}$, $\max\{|D_p(x)|\} \leq |N| \leq Area(I)$. $Area(I)$ indicates the area of the image. $|N|$ indicates a parameter which can take various values with the different models, and in this paper $|N|$ equals $Area(I)$. The weighted information of the energy functional is defined as follows:

$$W_{Ex} = \frac{|N|}{|D_p(x)|} \tag{13}$$

The weighted information of the kernel mapping function on the WKM model is defined as follows:

$$W_x = \frac{1}{|D_p(x)|} \tag{14}$$

Here W_{Ex} denotes the weight of energy functional at some pixels. Fundamentally, it can also be used as the weight of the step-size about the level set implementation at pixel x. In each iteration, the higher the value of W_{Ex} becomes, the faster it updates at pixel x. If the catchment basin is extremely small, then noises or outliers might exist and the corresponding weight of the level set will become large. Hence the updated level set element cannot give correct guidance to segmentation. In order to solve this problem, a threshold of the level set element is set to mitigate the influence of noise and outlier points. The value of W_{Ex} is greater than or equal to 1. When the weighted value of every level set element equals 1, it can be treated as traditional level set. As a consequence, the level set of the WKM model updates quicker than the traditional level set. W_x is used to indirectly express the weight of the kernel function. In each iteration, the region parameters are obtained by the weighted kernel function through using mean shift. The usage of W_{Ex} and W_x will be introduced in detail in next subsection.

4.3. The proposed energy functionals and the related level set formulations

In this research, two new energy functionals are designed to segment the image in the low dimensional observation space and the higher dimensional feature space respectively. The basic idea is that the problem of image segmentation can be transformed into the minimisation of an energy functional.

Let us define the evolving curve $\overrightarrow{\gamma}$ in Ω, μ_i expresses the parameter of the region R_i, and λ parameter is a positive factor. The new energy functional in the low dimensional observation space is defined as follows:

$$\int_{\Omega} \left| (p(x)\mu_1 + (1-p(x))\mu_2)(\frac{\mu_1+\mu_2}{2} - D(x) \pm \frac{\mu_1-\mu_2}{2}) \right| dx + \lambda \oint_{\overrightarrow{\gamma}} ds \quad (15)$$

The first term in Eq.(15) indicates the data term and the second term indicates the regularisation term in the low dimensional observation space, where $\pm$ depends on whether the point lies inside or outside the evolving curve, and the functional $p(x)$ is given by

$$p(x) = \begin{cases} 1, x \in inside(C) \\ 0, x \in outside(C) \end{cases} \quad (16)$$

Obviously, Eq.(15) can be described as follows:

$$E(R_1, R_1, \mu_1, \mu_2) = \int_{R_i} \mid \mu_i(\mu_i - D(x)) \mid dx + \lambda \oint_{\overrightarrow{\gamma}} ds \quad (17)$$

Whenever the evolving curve matches the boundary of the objective region, the energy functional can achieve a minimum value. So the proposed energy functional can transform the issue of image segmentation into that of energy minimi-

sation. It is assumed that the image is constructed by the foreground region and the background region, and every region has the same pixel value. Let us define the foreground region by R_1^0 and the background region by R_2^0 which are also used to express the segmentation result. Let us define regions R_1 and R_2, inside and outside the evolving curve respectively.

It is obvious that if R_1 is entirely inside the foreground area, then $E(R_1) = 0$ and $E(R_2) > 0$; if R_1 is partly inside the foreground area then $E(R_1) > 0$ and $E(R_2) > 0$; and so on. There are five possible cases in relation of the evolving curve and segmented region. The main remarks are illustrated in Fig. 3.

The new energy functional in higher dimensional feature space is defined as follows:

$$E_{K_w}(\Omega, \mu_1, \mu_2) = \int_\Omega W_{Ex} \mid (p(x)\phi(\mu_1) + (1 - p(x))\phi(\mu_2))(\frac{\phi(\mu_1)+\phi(\mu_2)}{2} - \phi(D(x)) \pm \frac{\phi(\mu_1)-\phi(\mu_2)}{2}) \mid dx + \lambda \oint_{\overrightarrow{\gamma}} ds \tag{18}$$

where $\phi()$ is a nonlinear mapping from the low dimensional observation space to the high dimensional feature space. Eq.(16) can be rewritten as

$$E_{K_w}(R_1, R_2, \mu_1, \mu_2) = \int_{R_i} W_{Ex} \mid (\phi(\mu_i))(\phi(\mu_i) - \phi(D(x)) \mid dx + \lambda \oint_{\overrightarrow{\gamma}} ds \tag{19}$$

Minimising E_{K_w} depends both on $\overrightarrow{\gamma}$ and region parameters μ_1 and μ_2, because the regularisation term does not depend on the region parameters, let

$$D_{K_w} = \int_{R_i} W_{Ex} \mid (\phi(\mu_i))(\phi(\mu_i) - \phi(D(x)) \mid dx \tag{20}$$

In this way, $\frac{\partial D_{K_w}}{\partial \mu_i}$ can be derived from $\frac{\partial E_{K_w}}{\partial \mu_i}$. According to the Mercer's theorem [33], any continuous, symmetric, as well as positive semi-definite kernel function can be expressed as a dot product in higher dimensional space, i.e. $K(y, z) = \phi(y)^*.\phi(z), \forall (y, z) \in D^2$. In this research, the RBF kernel function: $K(y, z) = \exp(- \parallel \frac{y-z}{\sigma} \parallel)$ is adopted. Hence

$$\frac{\partial D_{K_w}}{\partial \mu_i} = \int_{R_i} \frac{\partial}{\partial \mu_i} W_{Ex} \mid (K(\mu_i, \mu_i) - K(D(x), \mu_i)) \mid dx \tag{21}$$

The necessary condition for the minimum of E_{K_w} is $\frac{\partial D_{K_w}}{\partial \mu_i} = 0$, therefore,

$$\begin{aligned}\mu_{i,n+1} &= \frac{\int_{R_i} D(x) W_{Ex} K(\|\frac{D(x)-\mu_{i,n}}{\sigma}\|^2)dx}{\int_{R_i} W_{Ex} K(\|\frac{D(x)-\mu_{i,n}}{\sigma}\|^2)dx} \\ &= \frac{\int_{R_i} D(x) W_x K(\|\frac{D(x)-\mu_{i,n}}{\sigma}\|^2)dx}{\int_{R_i} W_x K(\|\frac{D(x)-\mu_{i,n}}{\sigma}\|^2)dx}\end{aligned} \tag{22}$$

Here, $i \in \{1, 2\}$, the sequence $\{\mu_{i,n}\}_{n=1,2,...}$ converges. The proof is given in Appendix A in the light of reference [16].

When region parameters are fixed and E_{K_w} is minimised with respect to $\overrightarrow{\gamma}$, the Euler-Lagrange descent equation corresponding to E_{K_w} is derived by embedding the curve $\overrightarrow{\gamma}$ into the family of one-parameter curves $\overrightarrow{\gamma}(s,t)\colon [0,1] \times R^+ \to \Omega$ and solving the following partial differential formulae:

$$\frac{d\overrightarrow{\gamma}}{dt} = -\frac{\partial E_{K_w}}{\partial \overrightarrow{\gamma}} \tag{23}$$

Segmentation region R_1 and R_2 are obtained from curve $\overrightarrow{\gamma}$ at convergence when time $t \to \infty$. Because E_{K_w} can be expressed by the integral of a scalar function, $\frac{\partial D_{K_w}}{\partial \overrightarrow{\gamma}}$ is equal to $-W_{Ex}(|\ (\phi(\mu_1))(\phi(\mu_1) - \phi(D(x)))\ | - |\ (\phi(\mu_2))(\phi(\mu_2) - \phi(D(x)))\ |)\overrightarrow{n}$ where $\overrightarrow{n}$ is the outward unit normal to $\overrightarrow{\gamma}$, the derivative of the length prior with respect to $\overrightarrow{\gamma}$ is $\frac{\partial}{\partial \overrightarrow{\gamma}} \oint_{\overrightarrow{\gamma}} ds = k\overrightarrow{n}$, we have

$$\frac{d\vec{\gamma}}{dt} = [W_{Ex}(|\ (\phi(\mu_1))(\phi(\mu_1) - \phi(D(x)))\ | - |\ (\phi(\mu_2))(\phi(\mu_2) - \phi(D(x)))\ |) - \lambda K]\overrightarrow{n} \tag{24}$$

The well-known level set method [34] is used here to evolve the curve $\overrightarrow{\gamma}(t)$ which is very stable. The topological changes of the evolving curve can be handled automatically. The curve is implicitly represented by the zero level set of function $u\colon R^2 \times R^+ \to R$ at time t, i.e., $\vec{\gamma}(t) = \{x \in \Omega \mid u(x,t) = 0\}$, $\frac{d\vec{\gamma}}{dt} = V_{K_w}\overrightarrow{n}$. When $V_{K_w}\colon R^2 \to R$, the corresponding level set function u evolves according to $\frac{\partial u}{\partial t}(x,t) = V_{k_w}||\overrightarrow{\nabla} u||$, therefore,

$$\begin{aligned}&\frac{\partial u}{\partial t}(x,t) = [W_{E_x}(|(\varphi(\mu_1))(\varphi(\mu_1) - \varphi(D(x)))| \\ &-|(\varphi(\mu_2))(\varphi(\mu_2) - \varphi(D(x)))|) - \lambda k_u]||\vec{\nabla} u||\end{aligned} \tag{25}$$

where the curvature function is given as follows:

$$k_u = div(\frac{\overrightarrow{\nabla} u}{||\overrightarrow{\nabla} u||}) \tag{26}$$

It should be noted that Eq.(25) is not only applied for points (x,t) on the curve

$\overrightarrow{\gamma}$ but also extended to the entire image region. In other words, the function u evolution is also suitable for points outside level set curve without affecting the process of segmentation. $\frac{\vec{\nabla} u}{||\vec{\nabla} u||}$ represents the unit normal to a level set curve at every point, and K_u represents the curvature of every level set element.

4.4. Main algorithm of WKM model for level set image segmentation

The main procedure of the proposed algorithm is summarised as follows:

Step 1: Initialise the level set evolution curves.

Step 2: Compute $\{\mu_\imath\}$ and K_u by Eq.(22) and Eq.(26), respectively.

Step 3: Update u by Eq.(25) and evolve the level set function according to step 2.

Step 4: Check the stopping criterion. If not, return to step 2.

Step 5: Output the final image segmentation results.

Note that the stopping criterion needs to be designed according to the practical problem. Therefore no unified stopping criterion is presented here.

Multi-region segmentation using several active curves can lead to ambiguity when two or more curves intersect. To address this problem, the method described in [16, 35] is adopted. The main idea is based on the following definition of a partition. If the segmentation has N regions, let $\{\overrightarrow{\gamma}_\jmath\}_{\jmath=1,\ldots,N-1}$ be N-1 simple closed plane curves and $\{R_{\overrightarrow{\gamma}_\jmath}\}$ be the enclosed regions, let $\{R_\jmath\}$ denote some partition regions, $R_1 = R_{\overrightarrow{\gamma}_1}; R_2 = R^C_{\overrightarrow{\gamma}_1} \bigcap R^C_{\overrightarrow{\gamma}_2}; \ldots; R_j = R^C_{\overrightarrow{\gamma}_1} \bigcap R^C_{\overrightarrow{\gamma}_2} \bigcap \ldots \bigcap R^C_{\overrightarrow{\gamma}_{\jmath-1}} \bigcap R^C_{\overrightarrow{\gamma}_\jmath}; \ldots;$ and $R_N = R^C_{\overrightarrow{\gamma}_1} \bigcap R^C_{\overrightarrow{\gamma}_2} \bigcap \ldots \bigcap R^C_{\overrightarrow{\gamma}_{\jmath-1}} \bigcap R^C_{\overrightarrow{\gamma}_{N-1}}$, where $R^C_{\overrightarrow{\gamma}}$ is the complementary of $R_{\overrightarrow{\gamma}}$ in Ω.

4.5. Complexity analysis of algorithm EWT and algorithm WKM

Complexity analysis for algorithm EWT: N indicates the total number of pixels in an image. To traverse every pixel, the complexity is obtained by calculating the complexity of 4-connected neighborhood search and 8-connected neighborhood comparison. At worst, a pixel is not determined as an extreme point by 8-connected neighborhood comparison, but it is added to different catchment basins twice by 4-connected neighborhood search. In this situation, the time complexity is O(16N). In Step 5, the second matrix is updated according to the first matrix, and the third matrix is updated by adopting the hash link-table, so the time complexity of updating three matrixes is O(3N). The step 4 is a selective step and its time complexity is O(8N), therefore, the time complexity of the extended watershed transformation is O(19N) or O(27N).

As discussed in Section 2.3, the complexity of every iteration of the KM model is $O(19N)$. Although the WKM model has one more process with the extended watershed transformation than the KM model, the WKM model requires much

fewer iterations than the KM model, so the time spent on the extended watershed transformation can be ignored.

In every iteration, the time complexity of the LIF model is $O((gl*gl+2*gw*gw+1)*N)$, the time complexity of the BCLBF model is $O((15+3*gn*gn)*N)$, and the MBCLBF model is more complex than the BCLBF model because of the local regional difference estimation in each iteration. Therefore the WKM model is superior to the LIF, BCLBF,and MBCLBF models as to the time complexity aspect.

5. Experimental results

To show the advantages of the proposed approach, quantitative and comparative performance evaluation is given including a large number of experiments on natural images from Berkeley database, medical images from Normal Brains Database as well as synthetic images with different characteristics. The proposed WKM model is compared with the aforementioned four models: Local Image Fitting (LIF) model [17], Bias Correction based Local Binary Fitting (BCLBF) model [18] and its modified model (MBCLBF) [22], as well as Level set image segmentation with Kernel Induced Data Term (KM) model [16]. In each experiment, the settings of initial curves and the parameters of each model are based on the recommendations of the original papers [16–18, 22]. Some parameters are slightly adjusted in order to get the better results. The settings of the parameters used in this research are shown in Table 1, Table 3, and Table 6.

5.1. Synthetic image segmentation

For synthetic images, we choose three images with different characteristics of noise: an image with much greater noise, an image with severe intensity inhomogeneity, and an image with narrow gaps. High contrast between the background and the foreground is the common feature among these three images. In Fig. 4, columns(a)-(e) show the segmentation results obtained by the BCLBF, LIF, KM, MBCLBF and WKM models respectively. Fig. 5 shows that the initial contours of every model are plotted on the original synthetic images, where the initial contours of the MBCLBF model are the same as the BCLBF model in column (a). The initial contours of the LIF model and the KM model are shown in column (b), column (c) respectively. The corrected images by the BCLBF method, the MBCLBF method and our EWT method are shown in Fig. 6. The same initial contours of the BCLBF, LIF, KM and MBCLBF models are chosen for the experiments of the WKM model, which are shown in the first column of Fig. 7, Fig. 8 and Fig. 9. The setting of parameters of each model is shown in Table 1. Unless

specified otherwise, apart from the parameters λ and d, other parameters of the WKM model are set to defaults in this section.

The first row of Fig. 4 shows an image with much greater noise than two other images and its segmentation results with curves can not be seen clearly. The last row shows the final segmentation regions in order to exhibit the segmentation result clearly. The BCLBF and MBCLBF models give the worse segmentation results than the LIF, KM and WKM models because the LFI function of the LIF model, the kernel function of the KM model can reduce the noise to a certain extent. Both the EWT method and the weighted kernel function of the proposed approach can reduce the noise significantly. As for the image with serious noise, the bias field of the BCLBF and MBCLBF models can not reduce the influence of noise. The corrected images by the BCLBF model and the MBCLBF model in Fig. 6 further explain the reason why these two models can not segment the images with stronger noise correctly. The column(c) of Fig. 6 shows that the EWT method reduces more noise than the BCLBF and MBCLBF models.

The second row of Fig. 4 shows an image with severe intensity inhomogeneity and noise. The BCLBF and MBCLBF models yield better segmentation results than the LIF and KM models because the bias field of the BCLBF and MBCLBF models is applied to deal with intensity inhomogeneity. The LIF and KM models may fail to extract the object boundary with severe uneven gray values and produce many local minima of the energy functional. because the EWT method can improve the homogeneity of an image and reduce the impact of noise, the WKM model can obtain better segmentation results than other four models.

The third row of Fig. 4 shows an image with narrow gaps and noise. Noise is the main cause of poor synthetic image segmentation. The LIF and KM models yield a litter bit better segmentation results than the BCLBF and MBCLBF models because the influence of narrow gaps is less than that of noise in high contrast image. The WKM model can produce more accurate segmentation results than other four models for the similar reason mentioned above. Fig. 7, Fig. 8 and Fig. 9 show that the WKM model with different initial contours can produce almost the same desirable segmentation results for the three synthetic images. The contour evolution processes are depicted by showing the initial contours, intermediate contours, and the final contours from the columns(a)-(e) of Fig. 7 and Fig. 8 as well as Fig. 9. This illustrates that the WKM model is insensitive to the initial contours. To sum up, the WKM model yields the best visual segmentation result for images with noise, narrow gaps and severe inhomogeneity with high contrast. Table 2 also shows that the WKM model can segment synthetic images with the fewest iterations.

5.2. Medical image segmentation

The medical images from Normal Brains Database [36, 37] are used to test the proposed WKM model. These brain images have the common features of narrow parts of the object with weak edges, a small amount of noise, inhomogeneity and low contrast between the background and the foreground. Because the KM model is not specifically used to segment the images with intensity inhomogeneity and low contrast, the segmentation results of the KM model for the brain images are very poor. Therefore, in this section, the WKM model is only compared with the LIF, BCLBF and MBCLBF models for the brain images. In Fig. 10, the first row shows the original brain images, and the second row shows the ground truth or gold standard for the brain images. In order to better compare the proposed model with other models, the segmentation error rate and Dice Similarity Coefficient (DSC) [38] are used to evaluate the performance of all models.

The segmentation error rate is computed as the ratio of the number of wrongly classified pixels to the total number of pixels in an image. Dice Similarity Coefficient (DSC) is defined as $DSC = \frac{2S(N_1 \cap N_2)}{S(N_1)+S(N_2)}$ where N_1 and N_2 represent the obtained segmentations, and $S(N_i)$ indicates the area of the region (N_i). The closer the DSC value turns to 1, the better the segmentation result will be.

In this section, we will discuss two-phase and three-phase image segmentation. We will not discuss three-phase image segmentation for the LIF model because it is not extended to be a multi-phase model. When evaluating the performance of all models, the accuracy for white matter (WM) in the brain is compared. The settings of parameters are shown in Table 3. Here, BCLBF2, LIF2, MBCLBF2 and WKM2 indicate the two-phase segmentation, BCLBF3, MBCLBF3 and WKM3 indicate the three-phase segmentation. Two-phase and three-phase segmentation results of BCLBF model are shown in the first row and the last row of Fig. 11. The initial contours of the LIF model are shown in the first row of Fig. 12. The initial contours of the BCLBF and MBCLBF models are also shown in the first row and the third row of Fig. 13. The corrected brain images by the BCLBF and MBCLBF models are shown in the middle row of Fig. 11 and Fig. 13. The segmentation results of the BCLBF, LIF, MBCLBF and WKM models are shown in Fig. 11, Fig. 12, Fig. 13, Fig. 14. Obviously the white matter segmentation results of BCLBF2 are worse than that of BCLBF3 in Fig. 11, the white matter segmentation results of MBCLBF2 are worse than that of MBCLBF3 in Fig. 11, we will choose the better segmentation results of the BCLBF and MBCLBF models to compare with the LIF and the WKM models. That is to say, we compare WKM2 and WKM3 with BCLBF3, LIF2 and MBCLBF3. The segmentation performances of BCLBF3, LIF2, MBCLBF3, WKM2 and WKM3 are compared in Table 4. According to Table 4, the segmentation performance

of the LIF model is a little bit better than that of the BCLBF model, the segmentation results of MBCLBF3 are superior to BCLBF3 and LIF2. The reason is that the MBCLBF model utilises the local regional difference to improve the bias field estimation of the BCLBF model. The WKM model achieves much better segmentation results and performance than the MBCLBF model because the EWT method can improve the intensity homogeneity of an image and the region parameters deduced by the WKM model can better represent the the intensity of the evolving regions. In Section5.3 we will illustrate how the region parameters of the WKM model can better represent the the intensity of the evolving regions. In other words, the WKM model is superior to the LIF, BCLBF and MBCLBF models for the brain images segmentation. Table 5 also demonstrates that the WKM model takes fewer iterations to finish the segmentation than the LIF, BCLBF and MBCLBF models.

5.3. Natural image segmentation

Compared to synthetic and brain images, natural images are often not artificially inhomogeneous but inherently inhomogeneous, and usually contain complex features. For instance, some natural images have the weak object boundaries but the strong (wrong) edges inside a target region. Because the segmentation results of the KM model for natural images are better than the LIF, BCLBF and MBCLBF models, in this section, the proposed WKM model is only compared with the KM model on natural images from Berkeley Database [39]. There exists neither ground truth nor gold standard on segmentation of the natural images. A set of benchmark segmentation results is used here, which is provided by four to seven human observers for each image and these benchmark segmentation results are publicly available [39–42].

There are four performance measures including Probabilistic Rand Index (PRI) [40], Variation of Information (VOI) [41], Global Consistency Error (GCE) [39], and Boundary Displacement Error (BDE) [42]. The PRI counts the fraction of pairs of pixels whose labels are consistent between the computed segmentation and the ground truth. The range of PRI is [0,1]. The higher value indicates the better result. The VOI measures the average conditional entropy of one segmentation given to the other. The range of VOI is $[0,\infty)$. The lower value indicates the better result. The GCE measures the extent to which segmentation can be treated as a refinement of the other. The range of GCE is [0,1]. The lower value indicates the better result. The Boundary Displacement Error (BDE)measures the average displacement error of boundary pixels between two segmented images. The ranges of BDE is $[0,\infty)$ in the unit of pixel, lower is better. We use the algorithms provided by Allen Y. Yang as mentioned in [43], to compute the four segmentation indices.

Fig. 15 shows nine natural images with initial contours from Berkeley database which are colour images in size 481×321. These images are selected in our experiments since they have been used as typical examples in many papers [16, 40–43] related to image segmentation. Table 6 lists the settings of parameters for the WKM and KM models. To compare the WKM model with the KM model fairly, initial contour of the WKM model for every natural image is the same as that of the KM model. Fig. 16 and Fig. 17 show the final segmentation results with curve representation. Column one, two and three of Fig. 16 and Fig. 17 show the two-phase, three-phase and four-phase natural images segmentation results respectively. The numerals underneath each of the natural images, such as 86016 and 35010, are the code names in Berkeley Database. In this section, we show the segmentation results and the segmentation performances to demonstrate the advantages of the WKM model on two-phase, three-phase and four-phase segmentation experiments. For the four-phase segmentation experiments, we also demonstrate the variation of the region parameters in iterations to further evaluate the effectiveness of the WKM model.

Column one of Fig. 16 and Fig. 17 shows that the WKM model can yield visually satisfactory segmentation results compared with the KM model. For image 86016 with serious noise and intensity inhomogeneity in the background as well as very high contrast between the foreground and the background, the KM model cannot segment the background well, whereas the WKM model provides proper or better segmentation result. Image 3096 has two segmented regions with complicated intensity inhomogeneity, strong edges in the background, and the weak edges from partial boundary between the foreground and the background. Image 80099 has severe intensity inhomogeneity and low contrast between the foreground and the background after gray transformation. Obviously, the WKM model can segment the foreground successfully, while the KM model cannot extract the boundary of the foreground correctly for image 3096 and image 80099. The reasons are that, firstly, our EWT method can significantly reduce the impact of the inhomogeneity and the noise, secondly, combining the the weighted kernel mapping function, the WKM model can overcome the influence of the wrong edges.

Column two of Fig. 16 and Fig. 17 illustrates the three-phase segmentation results of natural images obtained by the KM model and the WKM model. In Fig. 16, the results for image 183055 and image 118035 show that the KM model yields poor results in terms of four performance measures and gives the bad visual results. These two images have severe intensity inhomogeneity and contain strong edges inside the objective regions and weak edges from part of the boundary among the target regions after gray transformation. According to Fig. 17, the results for image 183055 and image 118035 show the WKM model can extract

the boundary of target regions successfully. According to Table 7 and Table 8, for image 238011, the WKM model and the KM model produce almost the same results in terms of the four performance measures. Image 238011 has high contrast among the target regions and has relative intensity homogeneity. However, the KM model fails to extract the moon area from image 238011 correctly and yields the boundary deviation. Since the moon area is a very small proportion of the whole image and the results of segmentation in other areas are desirable, the segmentation results obtained by both methods are satisfactory.

Column three of Fig. 16 and Fig. 17 shows the four-phase segmentation results of natural images obtained by KM and WKM respectively. Image 35010 is inhomogeneous and especially contains strong edges in the target regions. The WKM model can get competitive results comparing with the KM model from Table 7 and Table 8. As shown in Fig. 16 and Fig. 17, it is hard to judge which model is better for image 140075 and image 35010. However, the WKM model yields better results than that of the KM model in terms of PRI, BDE, VOI and GCE in Table 7 and autoreft8.

Table 9 shows the contrast of the KM model and the WKM model on the variations of four region parameters during evolutionary iterations. As can be seen in Fig. 18, the first row and the second row show the variations of four region parameters produced by the KM model and the WKM model for image 35010, image 140075 and image 124084 during the iterations. Because the KM model has very slow convergence rate, more iterations are required to get the desirable values of the region parameters. In this experiment, the iterations of the KM model are 5 times of the WKM model. Obviously, every region parameter obtained by the WKM model can converge quickly than that of the KM model. Meanwhile, since the image segmentation is spatially constrained clustering of image data, the more dispersed values of the region parameters mean the better performance. there is no doubt that the values of region parameters for the WKM model are more dispersed than that of the KM model.

Table 10 shows the contrast of the region parameters for image 35010, image 140075 and image 124084 by the KM model, the Benchmarks and the WKM model in low dimensional observation space. According to this table, the value of every region parameter by the WKM model is closer to the value of benchmarks than that of the KM model. Actually, this is one of main reasons that the WKM model can reach more accurate segmentation results than other models. However, it is surprised that the value of region parameter of image 35010, Region 3 by the WKM model is zero. The reason is that the corresponding region contains very few pixels and its corresponding intensity value is replaced by the EWT process. Since these pixels cannot influence the segmentation result due to the small quantity of the pixels, Region 3 of image 35010 can be ignored and the

four-phase segmentation is transformed into three-phase segmentation. Because the value of every region parameter by the WKM model in the low dimensional observation space is closer to the value of benchmarks than that of the KM model, and the values of region parameters for the WKM model in the higher dimensional space are more dispersed than that of the KM model, the region parameters deduced by the WKM model can better represent the the intensity of the evolving regions than that of the KM model.

Table 11 demonstrates that the proposed WKM model is much more efficient than the KM model in terms of iterations. Table 12 shows the quantitative comparison of the WKM model against the KM model on the VAL set of Berkeley Database, which indicates that the WKM model can produce better average performance in terms of BDE, VOI and GCE. It is remarkable that the KM model yields a little better performance than the WKM model in terms of the PRI on image 86016. However, the PRI is not the only criterion, and the segmentation result is not absolutely better when the PRI score is higher. An inverse example is given in Appendix B. Overall the WKM model outperforms the KM model on segmentation results of the natural images.

6. Conclusions

In this research, an Extended Watershed Transformation (EWT) method based on spring simulation is proposed and its algorithm is also presented. The EWT method can improve the image intensity homogeneity with almost no visual change. At the same time, the EWT method provides the weighted information for further level set image segmentation.

A Weighted Kernel Mapping (WKM) model for level set image segmentation is also proposed and its algorithm is presented as well. Two energy functionals in low dimensional observation space and higher dimensional feature space are proposed respectively. By combining the EWT method, the WKM model leads to better segmentation accuracy and iterative efficiency. According to the experiments on the synthetic images segmentation under high contrast between the foreground and the background, the brain images segmentation under lower contrast between the foreground and the background, as well as the complex natural images segmentation, all the results of these segmentations are sufficient to demonstrate the advantages of the WKM model. Compared with the popular LIF, BCLBF, MBCLBF and KM models, the WKM model has the minimum time complexity.

Because the texture features are not explicitly processed by the weighted kernel mapping function, the proposed WKM model cannot accurately segment the

texture images. Recently, an intensity-texture model [21] was introduced to segment texture images. However only two-phase texture images can be segmented. The first track for future work is to extend the WKM model to segment multiphase texture images by building a good texture term in the energy functionals. The extension of the proposed energy functionals for more new applications is also promising. Since the proposed method can deal with many types of images in an efficient way, another future perspective is to investigate the proposed method on big image segmentation.

Conflict of interest

None declared.

Acknowledgements

This work is supported by the grant from the National Natural Science Foundation of China, No.61033012.

Appendix A.

Let M_R be the mean shift update function defined in Eq.(21), the convergence of the following sequence equations is proved below

$$Z_{j+1} = M_R\left(Z_j\right) = \frac{\int_R D\left(X\right) K_W\left(D\left(X\right), Z_j\right) dx}{\int_R K_W\left(D\left(X\right), Z_j\right) dx}, j = 1, 2, \ldots \tag{A.1}$$

Here, R is a region within Ω and K_W is the weighted kernel function.

Because $K\left(x\right) = \exp\left(-x\right)$, sequence $\{Zj\}\, j = 1, 2, \ldots$ can be written as follows:

$$Z_{j+1} = \frac{\int_R D\left(X\right) W_x K\left(\left\|\frac{D(X)-Z_j}{\sigma}\right\|^2\right) dx}{\int_R W_x K\left(\left\|\frac{D(X)-Z_j}{\sigma}\right\|^2\right) dx}, j = 1, 2, \ldots \tag{A.2}$$

Let the sequence equations $\left\{P_\sigma\left(j\right)\right\}_{j=1,2,\ldots}$ be defined as follows:

$$P_\sigma\left(j\right) = \int_R W_x K\left(\left\|\frac{D\left(X\right) - Z_j}{\sigma}\right\|^2\right) dx, j = 1, 2, \ldots \tag{A.3}$$

The following proof demonstrates that the sequence $P_\sigma(j)$ converges and is a Cauchy sequence.

Since,

$$0 < W_x \leq 1, 0 < K\left(\left\|\frac{D\left(X\right) - Z_j}{\sigma}\right\|^2\right) \leq 1, \forall x \in R\, and\, R \subset \Omega \tag{A.4}$$

It will get

$$0 < P_\sigma(j) \leq \int_R dx \leq \int_\Omega dx \tag{A.5}$$

Thus, $P_\sigma(j)$ is bounded by the area of the image domain.

For $Z_{j+1} \neq Z_j, j = 1, 2, \ldots$ consider the following expression:

$$P_\sigma(j+1) - P_\sigma(j) = \int_R \left[W_x K\left(\left\| \frac{D(X) - Z_{j+1}}{\sigma} \right\|^2 \right) - W_x K\left(\left\| \frac{D(X) - Z_j}{\sigma} \right\|^2 \right) \right] dx \tag{A.6}$$

Because K is convex function, for all $u, v \in R^+ \, when \, u \neq v$, we have

$$K(v) \geq K(u) + K'(v - u) \tag{A.7}$$

For the properties of function K, we know $K(u) = -K'(u)$, then

$$W_x K(u) \geq W_x K(u) + W_x K(u - v) \tag{A.8}$$

Combined with (A.2), (A.6) and (A.8),

$$\begin{aligned}
&P_\sigma(j+1) - P_\sigma(j) \geq \int_R \left[W_x K\left(\left\| \tfrac{D(X) - Z_j}{\sigma} \right\|^2 \right) \times \left(\left\| \tfrac{D(X) - Z_j}{\sigma} \right\|^2 - \left\| \tfrac{D(X) - Z_{j+1}}{\sigma} \right\|^2 \right) \right] dx \\
&\geq \tfrac{1}{\sigma^2} \int_R \left[W_x K\left(\left\| \tfrac{D(X) - Z_j}{\sigma} \right\|^2 \right) \times \left(\|D(X) - Z_j\|^2 - \|D(X) - Z_{j+1}\|^2 \right) \right] dx \\
&= \tfrac{1}{\sigma^2} \int_R \left[W_x K\left(\left\| \tfrac{D(X) - Z_j}{\sigma} \right\|^2 \right) \times \left(2D(X) Z_{j+1} - 2D(X) Z_j + \|Z_j\|^2 - \|Z_{j+1}\|^2 \right) \right] dx \\
&= \tfrac{1}{\sigma^2} (2Z_{j+1}) \times \int_R \left[W_x D(X) K\left(\left\| \tfrac{D(X) - Z_j}{\sigma} \right\|^2 \right) \right] dx \\
&- \tfrac{1}{\sigma^2} (2Z_j) \times \int_R \left[W_x D(X) K\left(\left\| \tfrac{D(X) - Z_j}{\sigma} \right\|^2 \right) \right] dx \\
&+ \tfrac{1}{\sigma^2} \|Z_j\|^2 \times \int_R \left[W_x K\left(\left\| \tfrac{D(X) - Z_j}{\sigma} \right\|^2 \right) \right] dx \\
&- \tfrac{1}{\sigma^2} \|Z_{j+1}\|^2 \times \int_R \left[W_x K\left(\left\| \tfrac{D(X) - Z_j}{\sigma} \right\|^2 \right) \right] dx \\
&= \tfrac{1}{\sigma^2} 2 \|Z_{j+1}\|^2 \times \int_R \left[W_x K\left(\left\| \tfrac{D(X) - Z_j}{\sigma} \right\|^2 \right) \right] dx \\
&- \tfrac{1}{\sigma^2} 2 \|Z_j\| \|Z_{j+1}\| \times \int_R \left[W_x K\left(\left\| \tfrac{D(X) - Z_j}{\sigma} \right\|^2 \right) \right] dx \\
&+ \tfrac{1}{\sigma^2} \|Z_j\|^2 \times \int_R \left[W_x K\left(\left\| \tfrac{D(X) - Z_j}{\sigma} \right\|^2 \right) \right] dx \\
&- \tfrac{1}{\sigma^2} \|Z_{j+1}\|^2 \times \int_R \left[W_x K\left(\left\| \tfrac{D(X) - Z_j}{\sigma} \right\|^2 \right) \right] dx \\
&= \tfrac{1}{\sigma^2} \|Z_{j+1} - Z_j\|^2 \times \int_R \left[W_x K\left(\left\| \tfrac{D(X) - Z_j}{\sigma} \right\|^2 \right) \right]
\end{aligned}$$

It is to say that

$$P_\sigma(j+1) - P_\sigma(j) \geq \frac{1}{\sigma^2} \|Z_{j+1} - Z_j\|^2 \times \int_R \left[W_x K\left(\left\| \frac{D(X) - Z_j}{\sigma} \right\|^2 \right) \right] dx \tag{A.9}$$

Because $Z_{j+1} \neq Z_j, j = 1, 2, \ldots$, the right term in (A.9) is strictly positive, and consequently, the sequence equation P_σ is strictly increasing.

To sum up both sides in inequalities (A.9) over $j, j+1, \ldots, j+m-1$, it is given that

$$P_\sigma(j+m) - P_\sigma(j) \geq \frac{1}{\sigma^2}\|Z_{j+\mathrm{m}} - Z_{j+m-1}\|^2 \int_R W_x K\left(\left\|\frac{D(X)-Z_{j+m-1}}{\sigma}\right\|^2\right) dx$$
$$+ \cdots + \frac{1}{\sigma^2}\|Z_{j+1} - Z_j\|^2 \times \int_R W_x K\left(\left\|\frac{D(X)-Z_j}{\sigma}\right\|^2\right) dx$$
$$\geq \frac{1}{\sigma^2}\left[\|Z_{j+\mathrm{m}} - Z_{j+m-1}\|^2 + \cdots + \|Z_{j+1} - Z_j\|^2\right] M_{\min}$$
$$\geq \frac{1}{\sigma^2}\|Z_{j+\mathrm{m}} - Z_{j+m-1}\|^2 M_{\min}$$

So that:

$$P_\sigma(j+m) - P_\sigma(j) \geq \frac{1}{\sigma^2}\|Z_{j+\mathrm{m}} - Z_{j+m-1}\|^2 M_{\min} \tag{A.10}$$

Here $M_{\min}$ is the minimum of the integral $\int_R W_x K\left(\left\|\frac{D(X)-Z_{j+m-1}}{\sigma}\right\|^2\right) dx$ with respect to $\{Z_j\}_{j=1,2,\ldots}$.

Note that $M_{\min}$ is strictly positive, combined with inequalities (A.5) and (A.10), it can be concluded that P_σ is convergent, and is a Cauchy sequence. This result combined with (A.2) and (A.10) can conclude that $\{Z_j\}_{j=1,2,\ldots}$ is a Cauchy sequence. As a result $\{Z_j\}_{j=1,2,\ldots}$ converges in the Euclidean space.

Appendix B.

An inverse example of the PRI:

Let one image have only nine pixels and be segmented into three standard regions. These three regions are known as Tags. Tag one is indicated by bold font; Tag two is indicated by underlined font and Tag three is indicated by Italic font as shown in Fig. 19(a).

The count matrix is built by the benchmark segmentation results and from this we can compute the PRI and the GCE as shown in Fig. 19(b).(PRI=1,GCE=0)

We suppose two algorithms A and B, which are the respective segmentation algorithms. Fig. 19(c) shows the segmentation results based on algorithm A; Fig. 19(d) shows the value of count matrix A. (A:PRI=7/9,GCE=16/45) The segmentation results based on algorithm B is shown in Fig. 19(e) and the value of count matrix B is shown in Fig. 19(f)(B: PRI=5/6,GCE=2/5)

Although the PRI of algorithm B is bigger than that of algorithm A, visually, algorithm B produced worse segmentation result than algorithm A. The GCE of algorithm B is Also bigger than that of the algorithm A. Hence PRI is not the only criterion for image segmentation.

References

[1] J. M. Morel, S. Solimini, Variational methods in image segmentation, Birkhäuser Boston, Boston, MA, 1995.

[2] G. Aubert, P. Kornprobst, Mathematical problems in image processing, Springer, New York, 2006.

[3] D. Cremers, M. Rousson, R. Deriche, A review of statistical approaches to level set segmentation: Integrating color, texture, motion and shape, International Journal of Computer Vision 72 (2) (2007) 195–215.

[4] M. Kass, A. Witkin, D. Terzopoulos, Snakes: Active contour models, International Journal of Computer Vision 1 (4) (1988) 321–331.

[5] V. Caselles, F. Catté, T. Coll, F. Dibos, A geometric model for active contours in image processing, Numedsche Mathematik 66 (1) (1993) 1–31.

[6] R. Kimmel, A. Amir, A. M. Bruckstein, Finding shortest paths on surfaces using level sets propagation, IEEE Transactions on Pattern Analysis and Machine Intelligence 17 (6) (1995) 635–640.

[7] C. Xu, J. L. Prince, Snakes, shapes, and gradient vector flow, IEEE Transactions on Image Processing 7 (3) (1998) 359–369.

[8] A. Vasilevskiy, K. Siddiqi, Flux maximizing geometric flows, IEEE Transactions on Pattern Analysis and Machine Intelligence 24 (12) (2002) 1565–1578.

[9] C. Li, C. Xu, C. Gui, M. D. Fox, Level set evolution without re-initialization: a new variational formulation, in: 2005 IEEE Computer Society Conference on Computer Vision and Pattern Recognition, Vol. 1, IEEE, 2005, pp. 430–436.

[10] R. Ronfard, Region-based strategies for active contour models, International Journal of Computer Vision 13 (2) (1994) 229–251.

[11] C. Samson, L. Blanc-Féraud, G. Aubert, J. Zerubia, A variational model for image classification and restoration, IEEE Transactions on Pattern Analysis and Machine Intelligence 22 (5) (2000) 460–472.

[12] L. A. Vese, T. F. Chan, A Multiphase Level Set Framework for Image Segmentation Using the Mumford and Shah Model, International Journal of Computer Vision 50 (3) (2002) 271–293.

[13] T. F. Chan, L. A. Vese, Active contours without edges, IEEE Transactions on Image Processing 10 (2) (2001) 266–277.

[14] J. Lie, M. Lysaker, X.-C. Tai, A binary level set model and some applications to Mumford-Shah image segmentation., IEEE transactions on image processing : a publication of the IEEE Signal Processing Society 15 (5) (2006) 1171–1181.

[15] C. Li, C. Y. Kao, J. C. Gore, Z. Ding, Minimization of region-scalable fitting energy for image segmentation, IEEE Transactions on Image Processing 17 (10) (2008) 1940–1949.

[16] M. Ben Salah, A. Mitiche, I. Ben Ayed, Effective level set image segmentation with a kernel induced data term, IEEE Transactions on Image Processing

19 (1) (2010) 220–232.

[17] K. Zhang, H. Song, L. Zhang, Active contours driven by local image fitting energy, Pattern Recognition 43 (4) (2010) 1199–1206.

[18] C. Li, R. Huang, Z. Ding, J. C. Gatenby, D. N. Metaxas, J. C. Gore, A level set method for image segmentation in the presence of intensity inhomogeneities with application to MRI, IEEE Transactions on Image Processing 20 (7) (2011) 2007–2016.

[19] S. Liu, Y. Peng, A local region-based Chan-Vese model for image segmentation, Pattern Recognition 45 (7) (2012) 2769–2779.

[20] Y. Wang, S. Xiang, C. Pan, L. Wang, G. Meng, Level set evolution with locally linear classification for image segmentation, Pattern Recognition 46 (6) (2013) 1734–1746.

[21] H. Min, W. Jia, X.-F. Wang, Y. Zhao, R.-X. Hu, Y.-T. Luo, F. Xue, J.-T. Lu, An Intensity-Texture model based level set method for image segmentation, Pattern Recognition 48 (4) (2015) 1547–1562.

[22] C. Huang, L. Zeng, An active contour model for the segmentation of images with intensity inhomogeneities and bias field estimation, PloS one 10 (4) (2015) e0120399.

[23] D. Mumford, J. Shah, Optimal approximations by piecewise smooth functions and associated variational problems, Communications on Pure and Applied Mathematics 42 (5) (1989) 577–685.

[24] S. Zhou, J. Wang, S. Zhang, Y. Liang, Y. Gong, Active contour model based on local and global intensity information for medical image segmentation, Neurocomputing 186 (2016) 107–118.

[25] H. Wang, T.-Z. Huang, Z. Xu, Y. Wang, A two-stage image segmentation via global and local region active contours, Neurocomputing 205 (2016) 130–140.

[26] M. Girolami, Mercer kernel-based clustering in feature space, IEEE Transactions on neural networks 13 (PII S1045-9227(02)05003-83) (2002) 780–784.

[27] I. S. Dhillon, Y. Guan, B. Kulis, Weighted graph cuts without eigenvectors: A multilevel approach, IEEE Transactions on Pattern Analysis and Machine Intelligence 29 (11) (2007) 1944–1957.

[28] T. M. COVER, Geometrical and statistical properties of systems of linear inequalities with applications in pattern recognition, IEEE Transactions on Electronic Computers 14 (3) (1965) 326–334.

[29] L. Vincent, P. Soille, Watersheds in digital spaces: an efficient algorithm based on immersion simulations, IEEE Transactions on Pattern Analysis and Machine Intelligence 13 (6) (1991) 583–598.

[30] B. P. Dobrin, T. J. Viero, M. Gabbouj, Fast watershed algorithms: analysis and extensions, in: Proceedings of the Society of Photo-optical Instrumen-

tation Engineers, Vol. 2180, SPIE, 1994, pp. 209–220.

[31] A. Bieniek, A. Moga, An efficient watershed algorithm based on connected components, Pattern Recognition 33 (6) (2000) 907–916.

[32] M. Hammoudeh, R. Newman, Information extraction from sensor networks using the watershed transform algorithm, Information Fusion 22 (2015) 39–49.

[33] K. R. Müller, S. Mika, G. Rätsch, K. Tsuda, B. Schölkopf, An introduction to kernel-based learning algorithms, IEEE Transactions on Neural Networks 12 (2) (2001) 181–201.

[34] J. A. Sethian, Evolution, implementation, and application of level set and fast marching methods for advancing fronts, Journal of Computational Physics 169 (2) (2001) 503–555.

[35] A. R. Mansouri, A. Mitiche, C. Vázquez, Multiregion competition: A level set extension of region competition to multiple region image partitioning, Computer Vision and Image Understanding 101 (2006) 137–150.

[36] B. Aubert-Broche, M. Griffin, G. B. Pike, A. C. Evans, D. L. Collins, Twenty new digital brain phantoms for creation of validation image data bases, IEEE Transactions on Medical Imaging 25 (11) (2006) 1410–1416.

[37] B. Aubert-Broche, A. C. Evans, L. Collins, A new improved version of the realistic digital brain phantom, NeuroImage 32 (1) (2006) 138–145.

[38] D. W. Shattuck, S. R. Sandor-Leahy, K. A. Schaper, D. A. Rottenberg, R. M. Leahy, Magnetic Resonance Image Tissue Classification Using a Partial Volume Model, NeuroImage 13 (5) (2001) 856–876.

[39] D. Martin, C. Fowlkes, D. Tal, J. Malik, A database of human segmented natural images and its application to evaluating segmentation algorithms and measuring ecological statistics, in: Proceedings Eighth IEEE International Conference on Computer Vision, Vol. 2, IEEE, 2001, pp. 416–423.

[40] R. Unnikrishnan, C. Pantofaru, M. Hebert, A Measure for Objective Evaluation of Image Segmentation Algorithms, in: 2005 IEEE Computer Society Conference on Computer Vision and Pattern Recognition, IEEE, 2005, pp. 34–42.

[41] M. Meilă, Comparing clusterings: An axiomatic view, in: Proceedings of the 22Nd International Conference on Machine Learning, ACM, 2005, pp. 577–584.

[42] J. Freixenet, X. Mu, D. Raba, J. Mart, X. Cuf, Yet Another Survey on Image Segmentation : Region and Boundary Information Integration, in: Lecture Notes in Computer Science, Springer, 2002, pp. 408–422.

[43] A. Y. Yang, J. Wright, Y. Ma, S. S. Sastry, Unsupervised segmentation of natural images via lossy data compression, Computer Vision and Image

Understanding 110 (2) (2008) 212–225.

Tables and Figures

Table 1
Parameters setting of five models on synthetic images

methods	(a)	(b)	(c)
BCLBF	$\varepsilon = 1$; $\sigma = 14$;$mu = 1$;	$\varepsilon = 1$; $\sigma = 10$;$mu = 2$;	$\varepsilon = 0.8$; $\sigma = 8$;$mu = 1.5$;
	$nu = 0.001 * 255 * 255$;	$nu = 0.01 * 255 * 255$;	$nu = 0.001 * 255 * 255$;
LIF	$\varepsilon = 2$; $\sigma = 11$; G$\sigma = 1$;	$\varepsilon = 1$; $\sigma = 15$; G$\sigma = 5$;	$\varepsilon = 3$; $\sigma = 10$; G$\sigma = 1$;
KM	$\lambda = 20$; $\varepsilon = 1e - 10$;	$\lambda = 10$; $\varepsilon = 1e - 10$;	$\lambda = 20$; $\varepsilon = 1e - 10$;
	$\sigma = 10000$	$\sigma = 10000$;	$\sigma = 10000$;
MBCLBF	$\varepsilon = 1$; $\sigma = 5$;$mu = 1$;	$\varepsilon = 1$; $\sigma = 8$;$mu = 1.1$;	$\varepsilon = 0.8$; $\sigma = 11$;$mu = 1.2$;
	$nu = 0.007 * 255 * 255$;	$nu = 0.01 * 255 * 255$;	$nu = 0.01 * 255 * 255$;
WKM	$\lambda = 10$; $\varepsilon = 1e - 10$;	$\lambda = 1$; $\varepsilon = 1e - 10$;	$\lambda = 0$; $\varepsilon = 1e - 10$;
	$\sigma = 10000$;$d = 5$;	$\sigma = 10000$;$d = 3$;	$\sigma = 10000$; $d = 10$;

Table 2
Iterations of five models on synthetic images

methods	(a)	(b)	(c)
BCLBF	200	180	300
LIF	100	70	160
KM	40	60	45
MBCLBF	240	210	310
WKM	20	35	27

Table 3
Parameters setting of four models on brain images

methods	(a)	(b)	(c)
BCLBF	$\varepsilon = 1$; $\sigma = 3$;$mu = 1$;	$\varepsilon = 1$; $\sigma = 6$;$mu = 1$;	$\varepsilon = 1$; $\sigma = 6$;$mu = 1.5$;
	$nu = 0.001 * 255 * 255$;	$nu = 0.001 * 255 * 255$;	$nu = 0.001 * 255 * 255$;
LIF	$\varepsilon = 1$; $\sigma = 15$; G$\sigma = 0.3$;	$\varepsilon = 1$; $\sigma = 25$; G$\sigma = 0.6$;	$\varepsilon = 1$; $\sigma = 15$; G$\sigma = 0.7$;
MBCLBF	$\varepsilon = 1$; $\sigma = 15$;$mu = 1$;	$\varepsilon = 1$; $\sigma = 9$;$mu = 1.1$;	$\varepsilon = 1$; $\sigma = 9$;$mu = 1.2$;
	$nu = 0.004 * 255 * 255$;	$nu = 0.009 * 255 * 255$;	$nu = 0.008 * 255 * 255$;
WKM	$\lambda = 10$,$d = 5$;	$\lambda = 10$,$d = 5$;	$\lambda = 10$,$d = 5$;

Table 4
Performances of four models in terms of DSC and ErrorRate on brain images

methods	DSC			ErrorRate		
	brain1	brain2	brain3	brain1	brain2	brain3
BCLBF3	0.8089	0.7750	0.7849	0.1162	0.1489	0.1245
LIF2	0.8597	0.8586	0.8258	0.0826	0.0843	0.0975
MBCLBF3	0.9055	0.9027	0.8666	0.0522	0.0515	0.0689
WKM2	0.9268	0.9498	0.9479	0.0393	0.0259	0.0242
WKM3	0.9157	0.9379	0.9227	0.0427	0.0328	0.0369

Table 5
Iterations of four models on brain images

methods	brain1	brain2	brain3
BCLBF	80	65	90
LIF	55	40	60
MBCLBF	200	160	210
WKM	30	25	18

Table 6
Parameters setting of KM model and WKM model on brain images

image	86016	118035	35010	3096	238011	140075	80099	183055	124084
KM	λ=20;	λ=10;	λ=20;	λ=20;	λ=0;	λ=20;	λ=20;	λ=20;	λ=20;
WKM	λ=20;	λ=10;	λ=20;	λ=0;	λ=0;	λ=10;	λ=10;	λ=10;	λ=10;
	$d = 10$;	$d = 5$;	$d = 7$;	$d = 5$;	$d = 5$;	$d = 3$;	$d = 3$;	$d = 10$;	$d = 5$;

Table 7
Performances of the KM method in terms of the four measures on natural images

image	BDE	PRI	VOI	GCE
86016	24.6341	0.5330	2.8512	0.1982
118035	5.9042	0.7849	1.8585	0.1578
35010	6.3020	0.6539	3.7940	0.4050
3096	14.1129	0.8217	0.7294	0.0724
238011	1.2735	0.9362	0.4625	0.0527
140075	11.2946	0.5116	3.8818	0.5317
80099	27.2630	0.8241	0.6187	0.0414
183055	17.2096	0.6529	2.1148	0.2764
124084	9.9342	0.4707	2.9491	0.3081

Table 8
Performances of the WKM method in terms of the four measures on natural images

image	BDE	PRI	VOI	GCE
86016	23.8177	0.4978	2.2232	0.0114
118035	5.2991	0.8326	1.4472	0.0852
35010	6.0566	0.6566	3.7540	0.4004
3096	6.6405	0.8780	0.3950	0.0079
238011	1.2680	0.9403	0.4269	0.0477
140075	10.1736	0.6655	3.4296	0.4560
80099	11.8353	0.8896	0.3447	0.0089
183055	13.3802	0.7299	1.6537	0.1175
124084	5.7895	0.8017	2.0729	0.2193

Table 9
Contrast of KM model and WKM model on region parameter variation in iteration

N.	Image1(35010)								Image2(140075)								Image3(124084)							
	μ_{k1}	μ_{k2}	μ_{k3}	μ_{k4}	μ_{w1}	μ_{w2}	μ_{w3}	μ_{w4}	μ_{k1}	μ_{k2}	μ_{k3}	μ_{k4}	μ_{w1}	μ_{w2}	μ_{w3}	μ_{w4}	μ_{k1}	μ_{k2}	μ_{k3}	μ_{k4}	μ_{w1}	μ_{w2}	μ_{w3}	μ_{w4}
1	111.1	125.5	129.2	126.2	136.1	107.3	128.7	123.7	115.7	92.3	116.4	87.4	100.1	97.0	105.9	85.8	67.3	63.9	69.0	55.3	67.3	69.7	71.5	55.1
2	109.9	126.1	129.9	126.1	164.1	121.5	123.0	0.00	123.6	84.4	120.6	87.3	53.6	53.9	106.0	44.3	67.7	63.8	69.4	55.2	53.9	50.1	86.7	46.6
3	108.6	126.7	130.6	126.0	55.2	101.6	161.9	0.00	132.3	72.0	123.6	87.5	67.6	197.7	132.2	28.7	68.2	63.8	69.8	55.1	65.6	145.2	29.2	40.1
4	104.0	129.0	133.1	126.0	54.1	122.5	168.4	0.00	158.8	39.6	119.1	92.1	72.8	197.7	132.3	28.4	69.5	63.6	71.2	54.9	68.2	145.2	29.2	41.5
5	75.7	147.7	153.4	128.4	55.0	122.6	179.4	0.00	157.6	37.9	120.3	84.6	76.0	197.7	135.3	29.1	72.1	63.2	73.9	54.4	70.2	148.8	31.9	43.5
6	68.2	151.1	156.4	142.9	55.3	135.7	180.3	0.00	157.2	37.7	119.4	83.8	78.1	197.7	136.7	29.6	74.9	62.5	77.9	54.0	71.9	149.1	31.9	44.8
7	71.3	141.6	171.7	143.3	57.7	136.2	189.7	0.00	157.2	37.5	119.1	83.6	79.1	197.7	137.5	29.9	78.6	61.3	86.5	53.6	72.9	149.9	29.2	45.8
8	70.7	126.4	184.0	133.9	57.9	136.3	190.1	0.00	157.1	37.5	119.1	83.7	79.6	197.7	137.8	30.3	82.4	58.8	99.0	53.9	74.3	149.9	29.2	46.6
9	69.6	122.7	188.3	122.6	57.9	136.3	190.1	0.00	157.1	37.5	119.1	83.7	79.7	197.7	137.8	30.3	85.6	57.0	111.1	54.1	74.9	151.1	29.2	46.9
10	69.0	128.5	188.1	119.8	57.9	136.3	190.1	0.00	157.1	37.5	119.1	83.7	80.0	197.7	137.8	30.5	87.4	57.2	123.5	53.7	75.1	151.4	29.2	47.1
11	68.6	133.1	188.3	119.1	57.9	136.3	190.1	0.00	157.1	37.5	119.1	83.6	80.7	197.7	138.3	30.6	92.8	59.5	138.2	51.7	76.2	151.4	29.2	48.2
12	67.7	136.0	188.7	118.0	57.9	136.3	190.1	0.00	157.1	37.5	119.1	83.6	80.7	197.7	138.3	30.6	103.8	83.9	139.3	46.4	77.7	152.3	28.0	48.8

Table 10
Contrast of region parameters by KM, Benchmarks, WKM in low dimensional observation space

Region.	Image1(35010)			Image2(140075)			Image3(124084)		
	KM-lμ_i	BenchM-lμ_i	WKM-lμ_i	KM-lμ_i	BenchM-lμ_i	WKM-lμ_i	KM-lμ_i	BenchM-lμ_i	WKM-lμ_i
1	59.98	65.34	60.85	22.61	28.47	32.23	41.36	25.02	22.48
2	119.89	112.05	111.59	82.60	85.44	84.04	79.38	54.39	44.79
3	135.11	84.27	0	119.56	130.74	136.36	105.94	82.28	80.31
4	199.81	194.46	194.11	167.27	185.32	192.97	166.46	144.27	141.74

Table 11
Iterations of KM and WKM on natural images

image	KM	WKM
86016	66	30
118035	67	15
35010	132	13
3096	34	18
238011	96	9
140075	34	12
80099	152	27
183055	50	20
124084	150	14

Table 12
Average performances of WKM method against the KM method on natural images

methods	BDE	PRI	VOI	GCE
KM	25.9052	0.7049	3.0585	0.3478
WKM	22.1227	0.6908	2.8271	0.2304

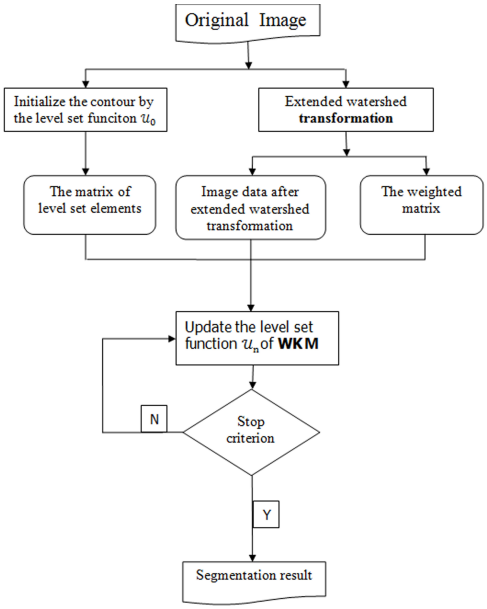

Fig. 1. Flowchart of the proposed image segmentation approach

Fig. 2. The result of the extended watershed transformation for image data with different values of d

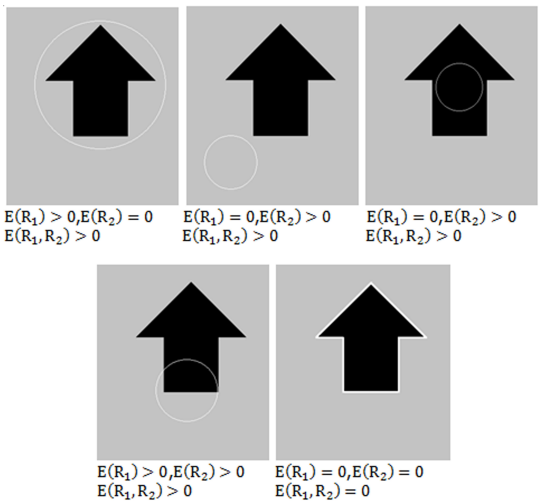

Fig. 3. All possible cases in relation of the evolving curve and segmented region. $E(R_1, R_2)$ achieves minimum only when the evolving curve makes $R_1^0 = R_1$ and $R_2^0 = R_2$

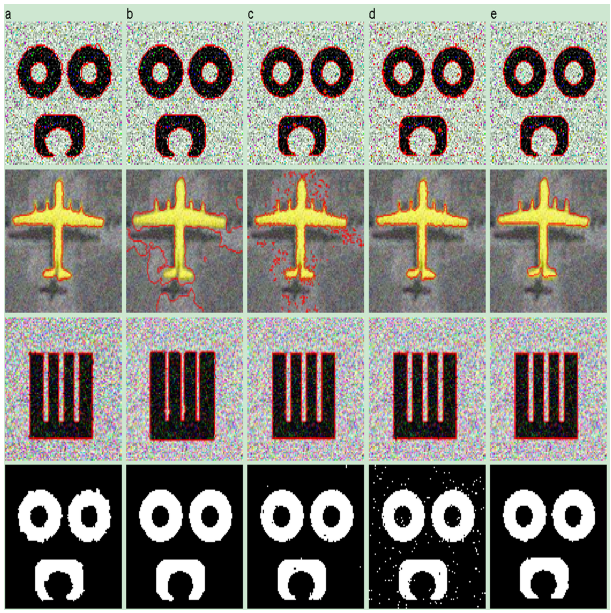

Fig. 4. Segmentation results on synthetic images obtained by BCLBF, LIF, KM, MBCLBF and WKM

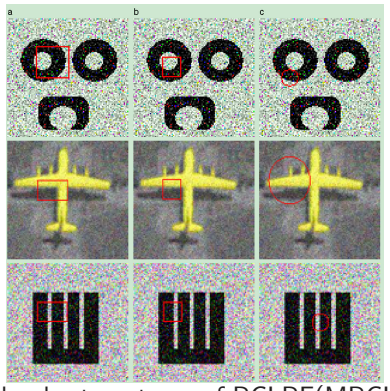

Fig. 5. Initial level set contours of BCLBF(MBCLBF), LIF, KM

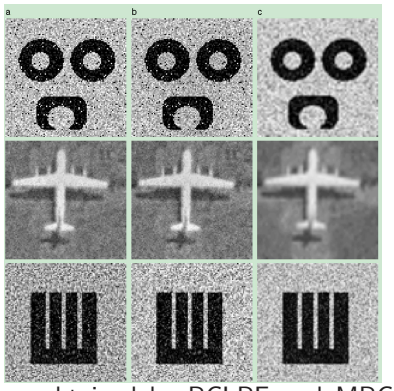

Fig. 6. Corrected images obtained by BCLBF and MBCLBF, and the extended watershed transformation result on synthetic images

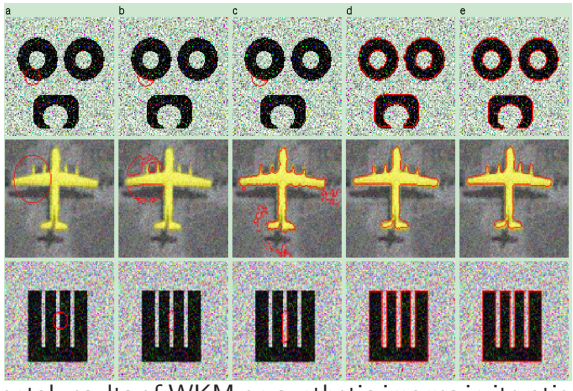

Fig. 7. Experimental results of WKM on synthetic images in iterations with the same initial contour as KM

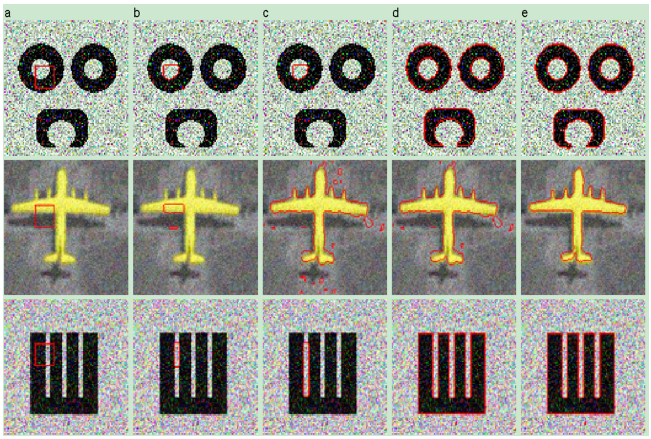

Fig. 8. Experimental results of WKM on synthetic images in iterations with the same initial contour as LIF

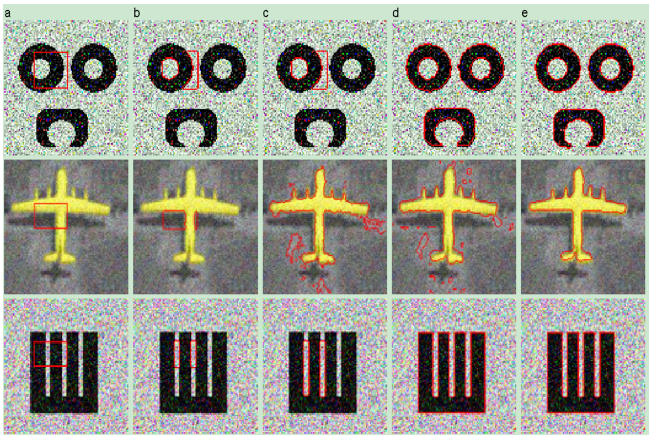

Fig. 9. Experimental results of WKM on synthetic images in iterations with the same initial contour as BCLBF and MBCLBF

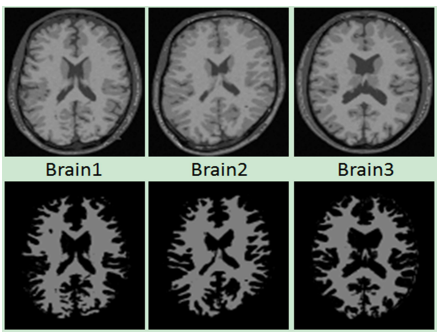

Fig. 10. Original images and ground truth on brain images

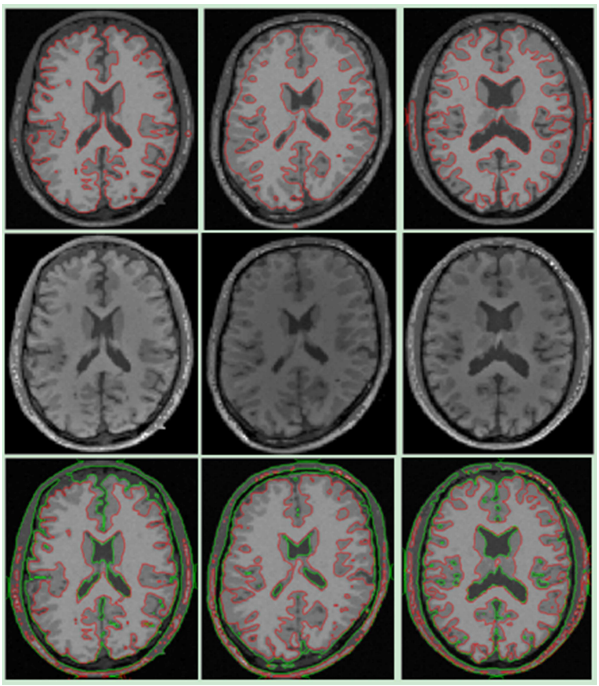

Fig. 11. Experimental results of BCLBF on brain images

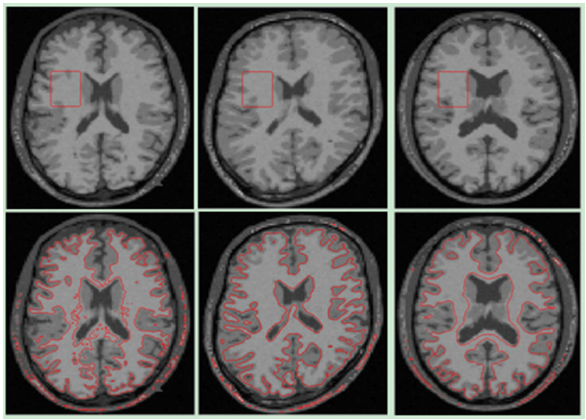

Fig. 12. Experimental results of LIF on brain images

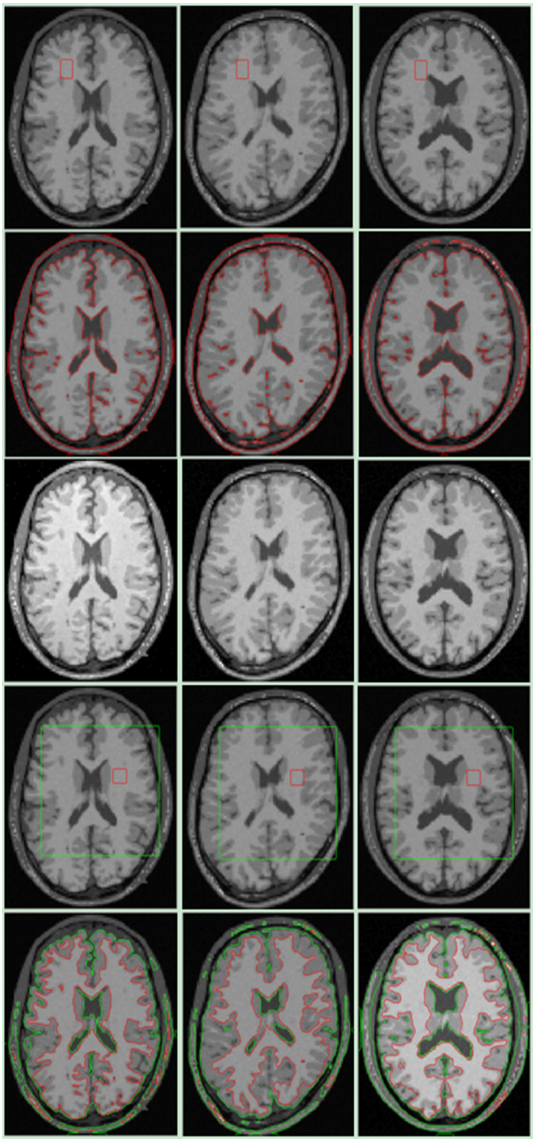

Fig. 13. Experimental results of MBCLBF on brain images

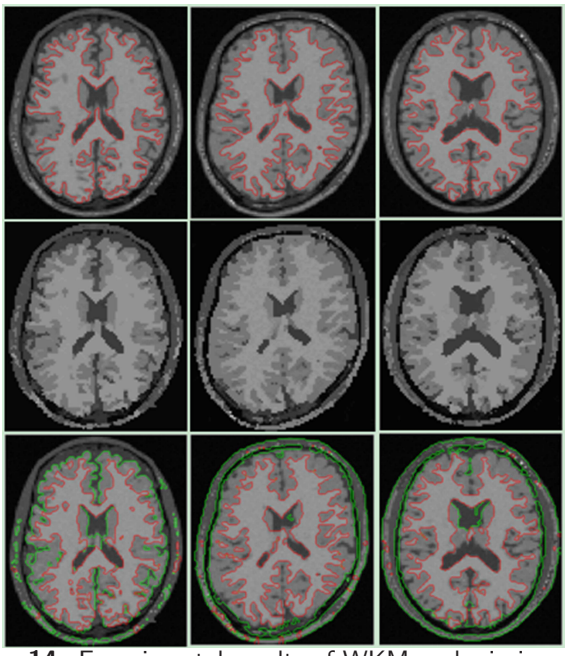

Fig. 14. Experimental results of WKM on brain images

Fig. 15. Natural images with different initial contours for two-phase, three-phase and four-phase segmentation

Fig. 16. Segmentation results of KM on natural images

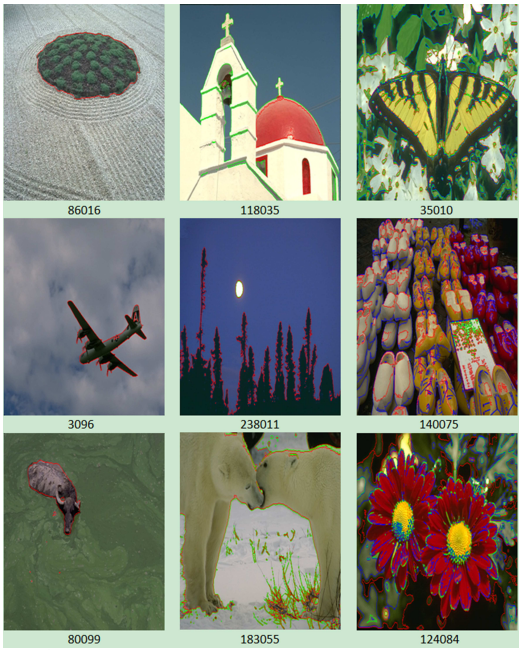

Fig. 17. Segmentation results of WKM on natural images

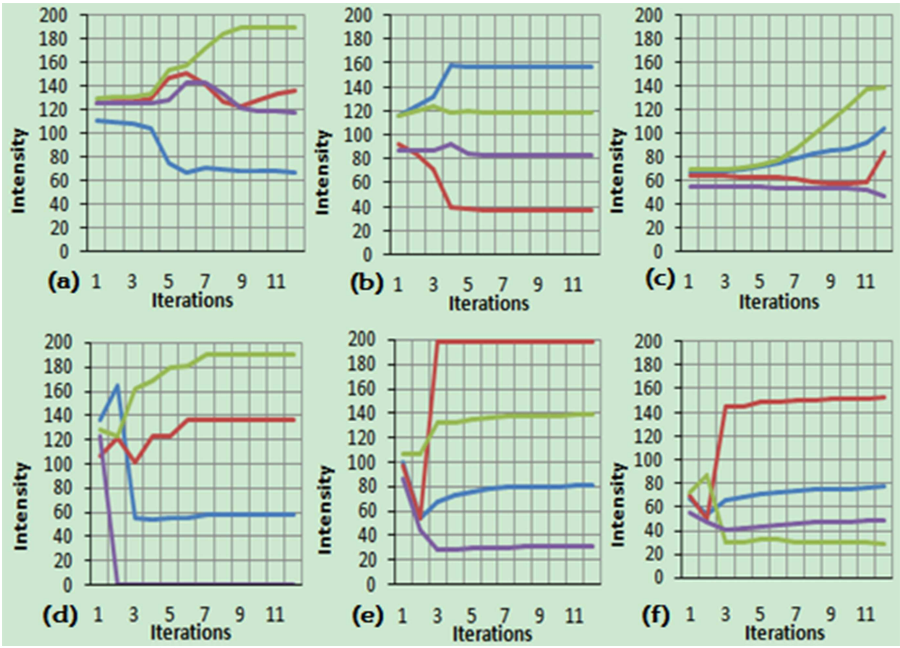

Fig. 18. Illustration of region parameters variation in iterations

20	30	**20**
26	30	*15*
26	*17*	**20**

(a)

5		
	2	
		2

(b)

20	30	*20*
26	30	*15*
26	*17*	*20*

(c)

1	**2**	**2**
	2	
		2

(d)

20	30	20
26	*30*	*15*
26	**17**	**20**

(e)

4	**1**	
	1	**1**
1		**1**

(f)

Fig. 19. the relative count matrices of the inverse example